The Influence of Cam Geometry and Operating Conditions on Chaotic Mixing of Viscous Fluids in a Twin Cam Mixer

Martin Robinson and Paul W. Cleary
CSIRO Mathematics, Informatics and Statistics Private Bag 33, Clayton South, Vic, 3168, Australia

DOI 10.1002/aic.12297
Published online June 23, 2010 in Wiley Online Library (wileyonlinelibrary.com).

Smooth particle hydrodynamica (SPH) simulations were used to better understand the mixing performance of a class of two-dimensional Twin Cam mixers. The chaotic manifolds of the flow are used to describe the mixing and to identify isolated regions. For an equilateral triangle cam geometry, a figure-eight manifold structure traps a layer of fluid against the cam boundaries. Changes in the differential rotation and phase offsets between the cams results in modest improvements in the mixing rate across the manifold barrier. Reducing the apex angle of the triangle changes the manifold structure and allows the trapped layer of fluid to mix more effectively with the rest of the domain. This article shows that examining the chaotic manifolds within a typical industrial mixer can provide valuable insight into both the transient and long-term mixing processes, leading to a more focused exploration of possible mixer configurations and to practical improvements in mixing efficiency. © 2010 American Institute of Chemical Engineers *AIChE J,* 57: 581–598, 2011
Keywords: chaotic advection, mixing, smoothed particle hydrodynamics, twin cam mixer

Introduction

Many industrial processes require the efficient mixing of highly viscous fluids. Examples include the production of paints, polymers, or food. The high viscosity of these fluids increases the power needed to operate the mixer since additional force is necessary to move the viscous fluid around the mixer, either via the motion of the impellors in a batch mixer or the pumping of fluid through a static mixer. The high viscosity also results in a laminar fluid flow due to the low Reynolds Number (*Re*). Without the benefits of turbulence, mixing is slow and limited by the molecular diffusivity of the fluids. It therefore becomes necessary to create many ''striations'' in the fluid via the continual application of stretching and folding operations[1] (i.e., a chaotic flow). These elongate material lines in the flow and increase the interfacial area between the different fluid components. The larger this area, the faster the diffusivity of the fluids can work to homogenize the contents of the mixer.

The aim of this article is to investigate the link between the impellor geometry/operating conditions and the structure of the chaotic manifolds/mixing processes within a particular class of Twin Cam mixers. In a previous article,[2] we validated the use of SPH simulation for such mixers using published FEM results and introduced tools used to extract manifolds and to quantitatively measure mixing. This article develops the manifold analysis methodology further, using these tools to help explore the fundamentals of the mixing process and how they respond to changes in geometry and operating conditions. Understanding these relationships is important for mixer design, and is a primary aim of this article.

Correspondence concerning this article should be addressed to M. Robinson at martin.robinson@csiro.au.

The Twin Cam mixer was chosen as a generic device that shares many attributes with the 3D mixers commonly used in industrial processes. In particular, it is comparable to a 2D cross-section of the popular Twin Screw Extruder. As the flow within this 3D mixer is predominantly cross-wise,[3] the use of a 2D model is a useful approximation to the 3D case. However, the aim of the article is not to optimize this specific 2D mixer, but to establish a base of understanding to support the use of this methodology for more complex 3D flows.

The Twin Cam mixer consists of a double-barreled outer boundary containing fluid and two rotating cams, one at each barrel center. An experimental and computational study of a Twin Cam mixer using equilateral triangular cams was performed by Avalosse and Crochet.[4] Bertand et al.[3] also simulated an identical Twin Cam mixer using a finite element simulation combined with a Lagrange multiplier based fictitious domain method to model the moving cam geometry. Both of these studies looked at a single cam geometry and operating conditions (co-rotating cams with equal angular velocity) whereas this study aims to explore the mixing under a variety of cam geometries and operating conditions. Jana et al.[5] analyzed the chaotic mixing within a vortex mixing flow (VMF), which is a similar but more idealized version of the Twin Cam mixer. It consists of a circular outer boundary containing fluid and two circular rotating cams. As the cams are circular, the chaotic flow in the VMF is generated by applying a time-varying relative angular velocity to the cams. In contrast, we have restricted the relative angular velocity of the cams to be constant, and the chaotic motion is generated by the stirring rotation of the (noncircular) cam boundaries.

Previously, we have used the meshless particle method smoothed particle hydrodynamics (SPH)[6] to simulate the same Twin Cam mixer of Avalosse and Crochet. Because of the Lagrangian nature of SPH, the advection of fluid is easily obtained from the movement of the SPH particles, removing the need to integrate large numbers of tracer particles in the flow. For time varying flow fields such as the Twin Cam mixer, this also eliminates the need to store large amounts of time-resolved velocity data. The SPH approach for modeling this system has been validated against finite element solutions[3,4] in the earlier article.[2]

Flows that exhibit chaotic trajectories can be divided into regions that exhibit different mixing characteristics. Regions containing regular, nonchaotic trajectories are permanently separated from the chaotic regions by Kolmogorov-Arnol'd-Moser (KAM) surfaces. These regular regions surround periodic elliptical points in the flow and need to be avoided to ensure a well-mixed domain over long timescales (i.e., thousands of periods). Poincare sections can easily show the location of these regular regions, and are often used as a first step in mixer design due to their low computational requirements.[5,7] The chaotic regions of the flow can be further classified, based on the chaotic manifolds that originate from periodic hyperbolic points in the flow. These manifolds are Lagrangian structures that separate regions with very different mixing characteristics. Hyperbolic periodic points are associated with strong stretching and folding of fluid regions, and the manifolds show the topological structure of these mixing actions. As they are material lines (or surfaces in 3D) that are advected along with the flow, these manifolds can also delineate regions that are isolated to some degree from the surrounding flow and therefore slow to mix with the rest of the domain. For more background on mixing and chaos in dynamical systems, consult books by Ottino[1] or Wiggens.[8]

This article investigates the short-term (up to 10 periods) mixing behavior in the Twin Cam mixer by examining the structure of the chaotic manifolds over time. The manifolds are ridges in the spatial map of Finite-Time Lyapunov Exponents[9] (FTLE). This method of locating the manifolds has a number of advantages over more traditional techniques.[10] A chaotic flow can have a very complicated manifold structure emanating from a number of periodic points. The length of each of these manifolds is infinite, so determining the periodic points and manifolds that are most important to the flow is a potential problem.[5] Using the spatial map of FTLE to find the manifolds, there is no need to manually locate and classify periodic points in the flow. Furthermore, the height of the ridges indicates the amount of stretching along the manifolds, which is a good measure of the importance of the manifold to the mixing.[5]

The FTLE is equivalent to the natural logarithm of Ottino's[1] length stretch, the global distribution of which is often used as a quantitative measure of mixing strength.[4,5,7] As the FTLE can be calculated for nonperiodic flows, they have been used to study flows in the atmosphere,[11] ocean,[9] or even biological cell evolution.[12] We have previously[2] developed a method to calculate the FTLE directly from SPH particle data, without the need to advect tracers in the flow.

To quantitatively compare the mixing between different mixer configurations, we have also followed the evolution of colored/dyed particles in the flow. We use a measure of mixing (defined in Robinson et al.[2]) that calculates the degree to which an initial colored region is mixed with the rest of the domain. This provides a practical measure that is directly related to the primary aim of any industrial mixer, the homogenization of fluid areas. In addition, the boundary of the initial colored region can be tuned to provide higher discrimination between mixer configurations. This is done by coloring regions that are slow to mix with the rest of the domain (these are easily identifiable from the manifold structure). An optimal mixing measure would be sensitive to these regions, as they define the ''worst-case'' mixing for the flow.

Methods

Smoothed particle hydrodynamics

SPH[6] is a Lagrangian particle method for simulating fluid flow. Rather than using a fixed grid, the method interpolates the fluid variables over a disordered set of particles, which move with the fluid velocity and as such it is well suited to mixing simulations. Each particle represents a volume of fluid, so it can have its own physical properties and the advection is obtained automatically from the motion of the particles.

The simulation of industrial mixers is often complicated by the use of complex moving geometries. SPH boundaries are constructed of particles which can be placed to follow the boundaries of any complex geometry, including sharp

corners.[13] Moving components such as impellors can be included in a simulation by assigning the appropriate velocity to each boundary particle.

The SPH formulation used for this article is identical to the one described in Robinson et al.[2] It is a quasi-incompressible method that uses an equation of state by Cole[14] and evolves the particle densities using the SPH version of the continuity equation. The traditional cubic spline kernel is used to interpolate the fluid equations across the particles and the viscous term used is described in Monaghan.[15] The no-slip boundaries are modeled using a single layer of boundary particles and the sharp corners are modeled using a multiple-normal technique proposed by Monaghan.[13]

For the purposes of this article, a Newtonian viscosity is used. However, the SPH method can also be used to model more complex fluid rheology, including shear-thinning, yield stress, and viscoelastic fluids. Many non-Newtonian fluids can be modeled with a Newtonian stress tensor and a variable viscosity. As the normal SPH formulation uses a variable viscosity for each particle, this is simple to implement and is the approach taken by Shamekhi et al.[16] and Shao and Lo,[17] who implemented Carreau and Cross viscosity models, respectively. The viscous term used in this article also ensures conservation of momentum in large gradients of viscosity. It is also possible to derive an SPH formulation using a generalized Newtonian stress tensor. Laigle et al.,[18] Rodriguez-Paz and Bonet,[19] and Hosseini et al.[20] all use this approach to implement Bingham or Herschel-Bulkley models. Finally, the Lagrangian nature of SPH is an advantage when modeling visco-elastic fluids, where the relationship between stress and strain depends on the time history of each particle. This avoids the need to perform back-integration along flow lines. Ellero and Tanner[21] derived an SPH stress term using a general Maxwell model and used it to simulate a Oldroyd-B and Upper-Convected Maxwell (UCM) visco-elastic flow.

The SPH method has a number of advantages in modeling mixing.

- No problems associated with mesh distortion between different moving components and between the moving and stationary components.
- The automatic advection arising from the Lagrangian formulation.
- The easy ability to accumulate the history of each piece of fluid. This allows easy calculations of the FTLE.

SPH has also proved to be a useful method for modeling several other classes of industrial applications. Cleary et al.[22] discusses the use of SPH in die casting, resin transfer molding, pyrometallurgical processes with reactive solids, slurry flow in sag mills, and the mixing of large particulate solids.

The primary drawback of SPH is that it is a relatively new method, and some aspects are not as proven in an engineering context as the more established methods such as FEM. In particular, areas such as turbulence modeling, non-Newtonian fluids and boundaries are still active areas of research. For applications that require the simulation of highly viscous fluid, SPH is potentially disadvantaged by the fact that it uses an explicit time-stepping scheme, which results in a small timestep size for large viscosities. However, in our previous article,[2] we have shown that a Twin Cam simulation at $Re = 10$ produced fluid transport that had no observable differences from experiments performed at lower Reynolds numbers, but resulted in a much more practical timestep size.

Chaotic manifolds and the finite-time lyapunov exponents

Chaotic dynamics define a stable manifold as a line (in 2D) or surface (in 3D) on which all the material points located on that manifold will approach its hyperbolic point (or line in 3D) as $t \to \infty$. This hyperbolic point (or line) is located at the intersection of a stable and an unstable manifold. An unstable manifold has the reverse property, whereby all the material points initialized on that manifold will approach its hyperbolic point in reverse time as $t \to -\infty$.

The important property of a stable manifold, from a mixing perspective, is that any small perturbation to a material point on the manifold will cause the particle to start moving exponentially away from the manifold. Over a finite time period, while the particle may stay close to the manifold, the (deforming) material line connecting the particle to the manifold will have an exponentially increasing length. Therefore, stable manifolds are associated with the stretching actions of the flow (See Figure 1). An unstable manifold has similar properties to the stable version, but in the reverse time direction. Practically, this means that material lines tangential to the unstable manifold have an exponentially increasing length and will become deformed along the length of the manifold. Therefore, unstable manifolds are associated with the folding actions of the flow (See Figure 1).

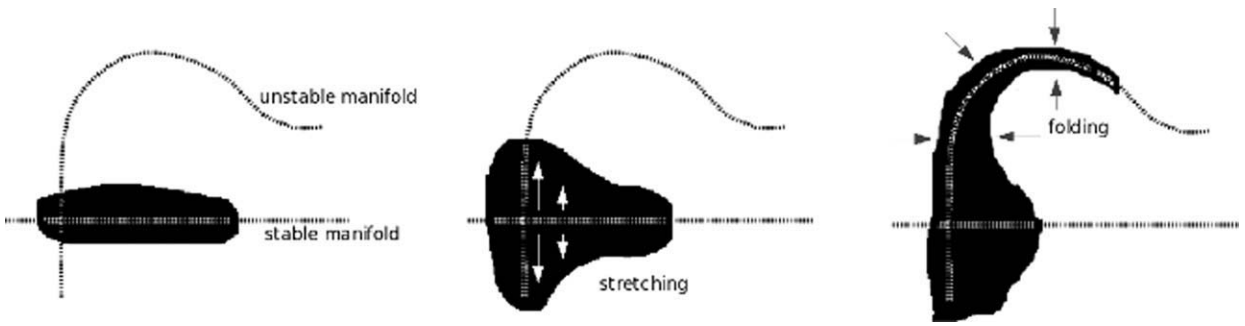

Figure 1. A stable and unstable manifold intersect at their hyperbolic point.

A patch of fluid will be stretched out tangentially away from the stable manifold, while also being elongated and folded along the length of the unstable manifold.

The geometry of the chaotic manifolds in a flow can be found by calculating a spatial map of the FTLE.[9] To do this, consider some initial material line segment of length **dx** at time t. At time $t + T$ this length has evolved to a new orientation and length **dX**. The traditional Lyapunov Exponent gives a measure of the exponential stretching of **dx** over an infinite time period and an infinitely small initial length

$$\sigma = \lim_{\substack{T\to\infty \\ |dx|\to 0}} \frac{1}{T} \ln \frac{\|\mathbf{dX}\|}{\|\mathbf{dx}\|} \tag{1}$$

The FTLE relaxes the infinite time condition and only considers the evolution of the flow over a finite time period T. The separation after time T, **dX**, will be

$$\mathbf{dX} = T \bigtriangledown \mathbf{v}\, \mathbf{dx} \tag{2}$$

where $\bigtriangledown \mathbf{v}$ is a first-order approximation of the velocity gradient over a finite time period T. In finite strain theory, $\mathbf{F} = T \bigtriangledown \mathbf{v}$ is known as the deformation gradient tensor. If $\lambda_{\max}$ is the absolute value of the maximum eigenvalue of $\bigtriangledown \mathbf{v}$, then

$$\lambda_{\max} = \frac{1}{T} \frac{\|\mathbf{dX}\|}{\|\overline{\mathbf{dx}}\|} \tag{3}$$

where the bar over **dx** indicates that it is aligned with the eigenvector corresponding to $\lambda_{\max}$.

Using the original definition of the Lyapunov Exponent, we can then define the Finite-Time Lyapunov Exponent σ as

$$\sigma = \frac{1}{T} \ln(\lambda_{\max} T). \tag{4}$$

Grid-based numerical methods use tracer particles to calculate the FTLE.[9,23] As the tracers can be initialized on a regular grid, finite-differencing can be used to estimate the spatial velocity gradient $\bigtriangledown \mathbf{v}$. For the Lagrangian SPH method, the SPH particles move with the local flow velocity and can be used directly. They will typically not be regularly spaced, so a least-squares method has been developed[2] to calculate the velocity gradient, whereby a linear fit of the velocity gradient is performed using the velocities of all the neighboring particles (i.e., all particles at a distance of $2h$ from the base particle, where h is the SPH kernel smoothing length and can be regarded as the minimum resolution of the SPH simulation).

Once the FTLEs have been calculated at every point in the domain, the stable and unstable manifolds of the flow are shown as ridges in the FTLE spatial map.[9] Unstable manifolds can be found from FTLE maps using a negative integration time $T < 0$ and stable manifolds can be found using $T > 0$. A ridge is a line of maximum FTLE in the direction along which FTLE has the greatest value of its second-order directional derivative. Manifold ridges can be extracted automatically from FTLE data using this definition.[9,24] However, for 2D applications such as the work presented in this article, a visual inspection of the FTLE spatial map is sufficient to distinguish the manifold structure.

Quantitative mixing

Although the structure of the chaotic manifolds of the flow provides insight into the topological nature of the mixing process, it is also useful to quantify the mixing so as to allow comparison of different mixing geometries. We use a measure that quantifies how well an initial dyed region of fluid is mixed into the rest of the domain. Many different such methods exist; however, most are application dependant. Poux[25] describes nearly 50 different mixing measures proposed in the literature. All of these measures calculate a global measure of how mixed two or more fluids are. In contrast, we use a local evaluation of the mixing which is described in Robinson et al.[6] This allows the calculation of the spatial variation in the degree of mixing, and a simple average can provide a global measure.

This mixing measure is defined as follows. Given a set of particles each having one of a possible C colors, the amount of mixing $M(\mathbf{x})$ measures how "mixed" the colors are using a particular length scale L. $M(\mathbf{x})$ is calculated at each point **x** in the domain, and the length scale defines a circular (or spherical in 3D) region around each point with a radius equal to L. All the particles within this subregion contribute to the amount of mixing at point **x**.

The mixing measure $M(\mathbf{x})$ is defined as:

$$M(\mathbf{x}) = \frac{\mathbf{s}_L(\mathbf{x}) \cdot \mathbf{s}_{\mathrm{g}} - M_{\min}}{M_{\min}} \tag{5}$$

where $\mathbf{s}_L(\mathbf{x})$ is a vector of the ratios of different colored particles in the local subregion. This subregion is defined as all the particles within a radius L from the point **x**. The global ratio $\mathbf{s}_{\mathrm{g}}$ is simply $\mathbf{s}_L(\mathbf{x})$ evaluated over the entire flow region ($\mathbf{s}_{\mathrm{g}}$ is therefore independent of **x**) and $M_{\min}$ is the minimum possible value of $\mathbf{s}_{L(\mathbf{x})} \cdot \mathbf{s}_{\mathrm{g}}$.

$$\begin{aligned} \mathbf{s}_L(\mathbf{x}) &= \frac{1}{\sqrt{\sum_{i=1}^{C} \left(\frac{n_i(\mathbf{x})}{N_i}\right)^2}} \left(\frac{n_1(\mathbf{x})}{N_1}, \frac{n_2(\mathbf{x})}{N_2}, \ldots, \frac{n_C(\mathbf{x})}{N_C}\right) \\ \mathbf{s}_{\mathrm{g}} &= \frac{1}{\sqrt{C}}(1, 1, \ldots, 1) \\ M_{\min} &= \frac{1}{\sqrt{C}} \end{aligned} \tag{6}$$

where $n_i(\mathbf{x})$ is the number of particles within radius L of **x** with color i, and N_i is the total number of particles in the simulation with color i.

This measure is invariant to translation and rotation of the spatial coordinate system. It changes linearly with the color ratios in the subregion and does not depend on the initial coloring of the particles, since $\mathbf{s}_{\mathrm{g}}$ is invariant. At large length scales equal to the entire domain, all the particles by definition are completely mixed [$M(\mathbf{x}) = 1$]. At length scales equal to the distance between the particles, the particles are completely segregated [$M(\mathbf{x}) = 0$].

The mixing measure $M(\mathbf{x})$ thus defined is a measure of how similar the color ratios within the local subregion are to the color ratios present in the entire domain. For example, consider an experiment in which an area equal to one quarter of the total domain area was assigned color 1 and the

remaining particles were assigned color 2. Points further than L away from the interface between the two areas will have $M(\mathbf{x}) = 0$ and the remainder will have $0 \leq M(\mathbf{x}) \leq 1$ depending on their distance from the interface. As the experiment continues the particles are mixed according to a chaotic flow that induces homogenous mixing of the particles. After a suitable time period, the particles will be fully mixed and all the points in the domain will have close to $N/4$ particles of color 1 and $3N/4$ particles of color 2 in their local subregion. This gives a mixing measure over the entire domain of $M(\mathbf{x}) \approx 1$.

It is often useful to plot M against the work done by the mixer to be able to provide a quantitative measure of the mixing efficiency. Given a rotating cam with angular velocity $\dot{\theta}$, the work done $W(t)$ by a force field $\mathbf{f}(\mathbf{x},t)$ over the cam boundary S is given by:

$$W(t) = \int_0^t \left\{ \oint_S \mathbf{x} \times \mathbf{f}(\mathbf{x}, t')dx \right\} \dot{\theta} dt'. \tag{7}$$

An equivalent discrete approximation to this equation is used to calculate $W(t)$ from the SPH particle data.

$$W(t) = \sum_{t'=0}^{t} \left\{ \sum_{a \in S} \mathbf{x}_a \times \mathbf{f}_a(t') \right\} \dot{\theta} \Delta t' \tag{8}$$

where $\mathbf{f}_a(t')$ is the total force on particle a at time t', Δt is the timestep and the inner sum is over all the boundary particles that make up the triangular cams.

Twin Cam mixer

In Robinson et al.,[2] we used SPH simulation to explore the mixing characteristics of a specific Twin Cam mixer with equilateral triangular mixing cams. The predictions were validated against published experimental[4] and numerical simulations.[3,4] The two impellers of the Twin Cam mixer are each in a separate, but connected, cylindrical barrel. These are shown diagrammatically in Figure 2.

The fluid used for the experiments was a Newtonian aqueous solution of glucose, with a viscosity of 50 Pa s and a density of 1500 kg/m^3. The counter-clockwise rotating cams are moving at 0.5 rpm, which gives a Reynolds number of the order of 0.001. The SPH method typically uses an explicit integration scheme, which gives very small time step for this type of system. Previously, in Robinson et al.,[2] it was shown that a lower viscosity of 0.005 Pa s, giving $Re = 10$, did not produce any observable difference on the flow dynamics when compared to either the experiment or lower Re solutions. The SPH results showed that the advection of the fluid was accurately calculated over a period of one cam revolution. Therefore, all the SPH simulations shown in this article use $\mu = 0.005$ Pa s.

The SPH simulation for this geometry uses an average particle separation of 0.75 mm. A total of 8637 particles were used in the simulation. In a previous article,[2] we determined that this particle resolution was sufficient to reproduce the fluid transport seen in published experiments and simulations of the Twin Cam mixer. All of the results presented in this article use an identical resolution, although the exact number of particles varies according to the area of the cam geometry. The CPU times for the SPH simulations range from 9 min (for Geometry 1) to 12 min (for Geometry 3) per 100 s of simulation time, on a single 2.5 GHz CPU.

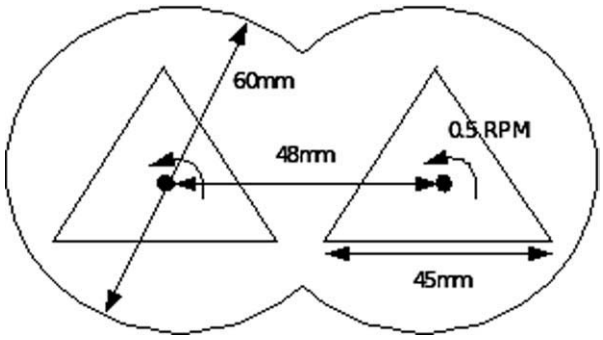

Figure 2. Geometry of the Twin Cam mixer with equilateral triangular cams.

The results of the SPH approach to modeling such mixing were validated using the experiment performed by Avalosse and Crochet.[4] Figure 3 shows the initial conditions for both the SPH simulation and experiment (top row), and the results after the cams have rotated through 1 revolution (middle row) and 1 1/3 revolutions (bottom row), taken at times 120 s and 160 s, respectively.

To visualize the mixing in the experiment, the authors dyed an initial area of fluid, shown in Figure 3 (right top) as an approximately elliptical black area in the center of the domain. A similar area of fluid is shown in the SPH results in the left column. To compare the SPH results with the experiment only dyed particles are shown.

As the cams rotate, they divide the dyed area into two segments along a line that is roughly diagonal from the lower right tip of the left cam to the top of the right cam. Fluid particles above this line are advected into the left barrel of the mixer while the rest move into the right. Once divided, the majority of the fluid particles are stretched out into a rough line due to the motion of the cam walls and the lower velocities near the walls of the chamber. There is a stationary point at the center of the domain, so the fluid particles near this point have a reduced velocity. This causes a thinning trail of dye as they leave the center of the domain, which subsequently shortens to form a hook-like structure, which can be seen most clearly in the lower region of the leftmost chamber at $t = 120$ s (Label "A" in the figure). A similar structure is formed near label "B" in the right barrel.

Once the leading edges of the dyed region have completed a revolution and are once again near the center of the domain, both are divided again along the same line as before. This can be seen near label "C" in the $t = 160$ s plot, where T-shaped structures are being formed as the fluid particles are forced in a direction perpendicular to their original motion.

The motions of the dark particles in the SPH simulation follow that of the dyed experimental area well over a period of one cam revolution. After this time period, the particles have completed a circuit around either the left or right cam and have returned to the center of the mixer. Here, small deviations from the experimental results are amplified due to the highly chaotic central region.

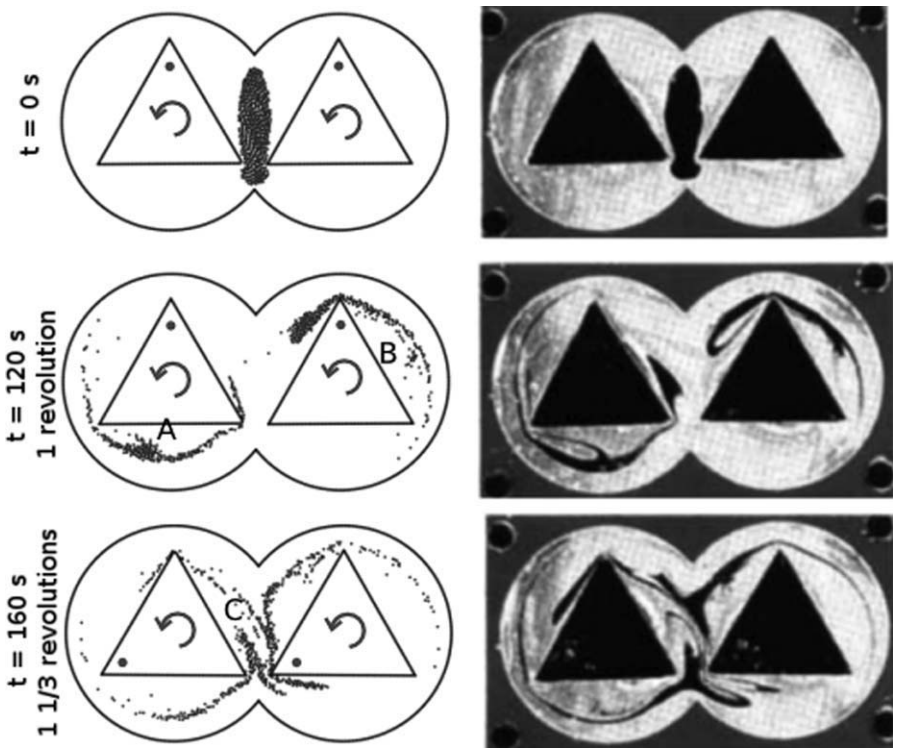

Figure 3. Comparison of SPH simulation with the experimental results from Avalosse and Crochet.[4]

Manifold evolution

Figure 4 shows the geometry of the unstable and stable manifolds of the flow. These were calculated in Robinson et al.[2] by tracing the ridges in the forward and backwards time FTLE maps using $T = \pm 120$ s (T is the finite-time period over which the particle are tracked before the FTLEs are calculated). They are reproduced here to describe the manifold geometry and how this relates to the mixing processes in the Twin Cam mixer.

The stable manifolds are shown as dark gray curves. They are associated with the stretching apart of fluid areas. The primary source of this stretching is the hyperbolic point at the center of the domain, where the two manifolds intersect. Closer to this point, the "strength" of the manifold is greater and particles move apart faster. Further away, the stretching effects are weaker, but the geometry of the manifolds is still relevant in that they divide the domain into regions with significantly different dynamical evolution. Consider the fluid particles shown in the top diagram of Figure 4. The stable manifold intersects this region, dividing these particles into two sets. Those above this line will move upwards, perpendicularly away from the manifold and into the left barrel of the mixer. The particles below this line will move in the opposite direction and are transported into the right barrel of the mixer.

The unstable manifold is associated with the folding action of the mixing and is shown as the light gray curve in Figure 4. Fluid areas near this line will become elongated and are folded along the length of the manifold. Considering again the fluid particles shown in Figure 4, the plots at $t =$ 25 s and 50 s show that the fluid area defined by these particles becomes elongated along the path defined by the unstable manifold.

Taken together, these two manifolds form a thin tangle in a roughly figure eight structure around the two cams of the mixer. The pair of manifolds intersects each other at a number of points around the cams, delineating a set of fluid "lobes" that are encircled by the manifolds between each of the intersection points. The rate of fluid transport across the tangle of manifolds is proportional to the area of these lobes.[26] As the manifolds become closer to coincident, the tangle represents a stronger barrier to transport. A well designed mixing flow would be characterized by a homogenous distribution (spatially and/or over time) of manifolds throughout the domain, with no single region surrounded by a persistent thin tangle of stable and unstable manifolds. However, in the case of the Twin Cam mixer, the structure of the tangle does not change over time and the area of the lobes is small compared to the total area of the mixer. Therefore, the transport of fluid across this barrier is slow, and the figure eight geometry of the manifolds means that the fluid between the tangle of manifolds and the cam walls will be substantially isolated and will not mix efficiently with the rest of the domain.

The figure eight structure of the manifolds clearly defines a dead zone in the Twin Cam mixer. In Robinson et al.[2] it was shown that after eight revolutions of the cams, the amount of mixing (according the mixing measure M) between this zone and the rest of the domain is half that of the overall mixing from one barrel to the other. The identification of these dead zones in a mixer is important for mixer optimization. The geometry of the manifolds clearly defines the location and structure of these zones. Furthermore, the manifolds show how the

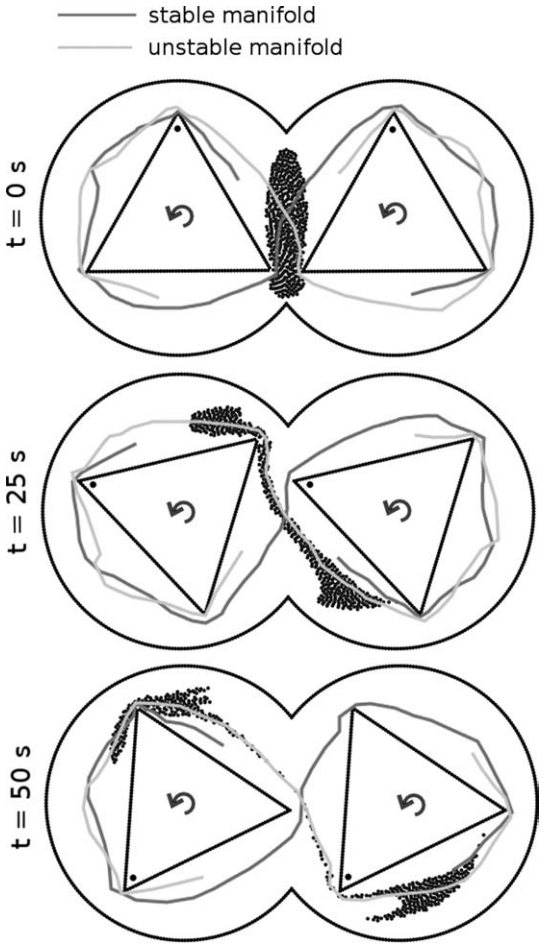

Figure 4. The initial colored area of fluid surrounding the hyperbolic point is stretched and torn apart along the line of the stable manifold.

It is then folded around the cams following the unstable manifold.

fluid is being transported around the mixer and allows greater insight into the mixing processes.

Effects of integration time on FTLE estimation

Spatial maps of FTLE describe the dynamical evolution of each particle over the time period t_0 to $t_0 + T$. There are two time parameters associated with these maps, the initial time t_0 and the period T over which the particles are tracked. The FTLE map gives a picture of the dynamics of the particles over a time period T. Manifolds that exist during this time will appear as ridges in the FTLE map with lengths roughly proportional to $|T|$. To illustrate the dependence of ridge length on $|T|$, Figure 5 shows two particles at $t = t_0$ and $t = t_0 + T$. They are initially on either side of a stable manifold and as they move closer to the hyperbolic point, they diverge and start following the unstable manifold in opposite directions. It can be seen that as long as T is large enough that the two particles reach the vicinity of the hyperbolic point and diverge, then a large value for the FTLE will be calculated at the initial location of the particles. An identical result would occur in reverse time for two particles initialized straddling the unstable manifold.

Figure 6 shows the FTLE maps using $T = -24$, -72, -120, and -192 s. Ridges in these maps correspond to unstable (attracting) manifolds. For $|T| \leq 120$ s, only the length of the ridges changes, growing with increasing $|T|$. Therefore, it is natural to conclude that a larger value of T is beneficial in that it reveals more of the manifold geometry. However, increasing $|T|$ too much can result in FTLE maps that are noisy and difficult to interpret due to errors inherent in the long-term FTLE estimation. The calculation of the FTLEs assumes that the Lagrangian velocity gradient for each particle is approximately constant, resulting in the initially circular neighborhood of particles becoming stretched out in a single direction, but still remaining a coherent group over time. Consider the particle pair shown in Figure 5. Over the time period T given in this diagram, the pair separates relative to each other only in one direction (perpendicular to the stable manifold). Increasing T further might lead to one or both of the particles passing near another hyperbolic point with its own set of manifolds, which would dramatically change the estimated FTLE. Alternatively, over time the flow could simply move the particles closer together, which is inevitable with a closed system. The problem is compounded due to the fact that the FTLE estimate uses a circular region of particles instead of a single pair. This region will become increasingly distorted over time, particularly if it passes near more than one hyperbolic point.

For $|T| \leq 120$ s, the estimation of the FTLE remains accurate and the manifold geometry is clear to see. For T greater than this, the maps become increasingly noisy. However, it is still useful to view the FTLE maps for larger values of T. Most notably, the FTLE map within the dead zone close to the walls of the cams always remains low compared with the rest of the domain. Even though the geometry of the manifolds is unclear for $T > 120$ s, it is useful to know that they never move into the isolated central dead regions surrounding each cam.

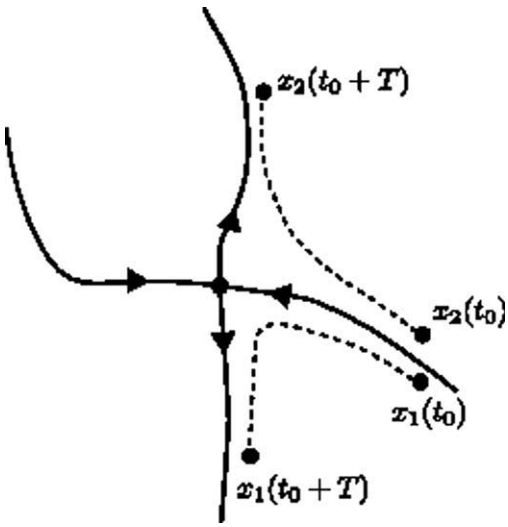

Figure 5. Two particles shown at $t = t_0$ and $t = t_0 + T$.

The particles are initialized near the stable manifold and eventually diverge to follow the unstable manifold along opposite directions. As long as T is large enough that the particles diverge, then large values of FTLE will be calculated at the two initial positions.

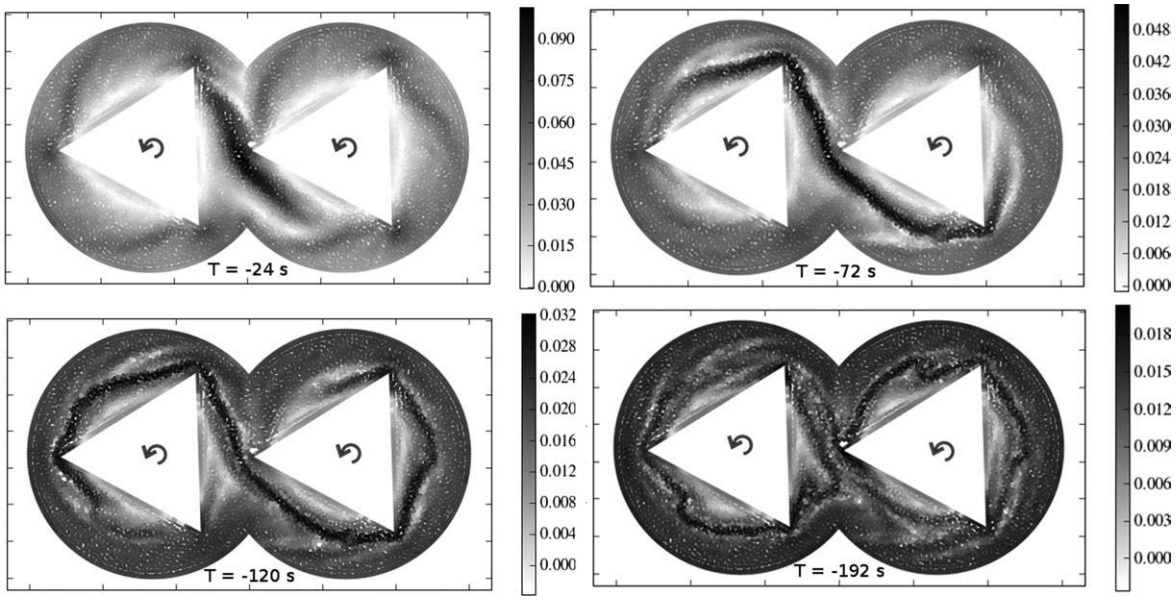

Figure 6. Backwards time FTLE map with $T = -24$, -72, -120, and -192 s.

The lengths of the manifolds are governed by $|T|$. A point at the end of the manifold will approach the central hyperbolic point as $t \rightarrow T$.

In general, an optimal value to choose for T will be slightly less than the minimum time for a fluid particle to move from one hyperbolic point to another in the mixer. For the case of the twin cam mixer, there is only one hyperbolic point, and the time taken for any fluid particle near this point to be transported around the cams and back to the same hyperbolic point will be greater than or equal to the cam period (120 s). Taking $T = 120$ s will therefore reveal the maximum amount of the manifold structure, without introducing an unacceptable level of error into the FTLE map.

Effect of varying mixer operating conditions

Often the easiest and cheapest way of optimizing the mixing process is to alter the mixer controls. Changing the relative speed or phase of each triangular cam is straightforward and does not require alteration of the fundamental operation or structural change of the geometry of the mixer.

The different operating conditions were compared using the measure of mixing $M(\mathbf{x})$ introduced in Eq. 5. In all cases, the length scale L was taken to be $L = S/32 = 3.75$ mm, where S is the width of the mixer. This ensures a sufficient number of particles within each subregion (78) so that $M(\mathbf{x})$ varies smoothly across the domain, while still providing an adequate spatial resolution. The results are qualitatively similar for other length scales (sufficiently far from both the particle length scale and the domain scale) and are representative of the general mixing behavior on several scales.

The evolution of the amount of mixing $M(\mathbf{x})$ depends on how the fluid is separated into different regions.[2] In other words, $M(\mathbf{x})$ depends on the initial distribution of colors over the domain. Differing regions will intermingle at different rates depending on how their geometry relates to the geometry of the chaotic manifolds. For example, consider two different divisions of the fluid in the mixer. The first divides the mixer down the middle, defining each barrel of the mixer as a separate region, and measuring the mixing exchange of fluid between barrels. The second separates the fluid into two regions, one between the figure eight tangle of manifolds and the cam boundaries, the other filling the remainder of the domain. As the flux of material across the chaotic manifolds is slow, this division will experience significantly slower mixing between the two regions than the first. Figure 7 shows the time evolution of $M(\mathbf{x})$ for the two divisions [$M_1(\mathbf{x})$ refers to the inter-barrel mixing while $M_2(\mathbf{x})$ refers to the cross-manifold mixing]. For $M_1(\mathbf{x})$, the particles are colored at $t = 0$ s so that the particles in the left barrel are assigned color 1, while those in the right barrel are given assigned color 2. For $M_2(\mathbf{x})$, the particles closer than 22 mm from the center of each barrel (hereafter termed the ''inner'' region) are assigned color 1 and the remainder are assigned color 2 (the ''outer'' region).

The mixing plots at $t = 0$ s show the interface between the two regions as a ridge in $M(\mathbf{x})$. As time increases, the interface shown in $M_1(\mathbf{x})$ (top row) is elongated and is soon hard to resolve as it quickly becomes deformed and passes beyond what can be captured by the finite resolution of the particles. By the end of the simulation ($t = 637$ s), the outer region of the mixer is almost completely mixed and there is only an inner region close to the cam boundary that is unmixed. Defining ''unmixed'' as $M(\mathbf{x}) < 0.8$ (an arbitrary but reasonable definition) this region is 24% of the total mixer area. The second row shows $M_2(\mathbf{x})$, which measures the amount of mixing between the inner and outer regions. Over time, the interface between these two regions grows only slightly as the particles near the interface are barely mixed. By the end of the simulation, there is only weak mixing between these two regions. The difference in the mixing observed for the two different color schemes highlights the extent of the variation of the mixing and the importance of measuring the mixing in the slowest mixing regions.

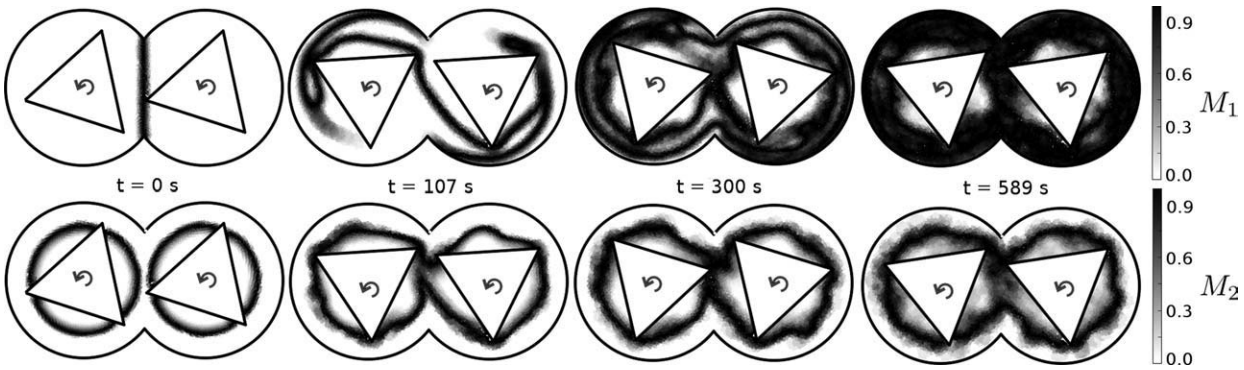

Figure 7. Top row: Mixing measure M_1(x), which measures the amount of mixing between the two barrels of the mixer; bottom row: Mixing measure M_2(x).

This measures the amount of mixing between the inner and outer regions of the mixer.

Although it is useful to see how the mixing varies throughout the domain, a global measure is needed to properly compare different mixer operating conditions. $\hat{M}_1$ and $\hat{M}_2$ are the mean values of $M_1(\mathbf{x})$ and $M_2(\mathbf{x})$, where the mean is taken over the entire domain. These two measures are used for quantitative comparison. As the energy used to operate the mixer is an obvious concern, $\hat{M}_1$ and $\hat{M}_2$ are plotted against the total work done $W(t)$ by the mixer, rather than time. This is done because we are more interested in changes of mixing efficiency rather than absolute changes in mixing time.

Five different cases of operating conditions for the mixing, involving differential rotation rates and phase offsets between the cams, were evaluated:

1. The base case where both cams start with a relative phase of zero radians and move with an angular velocity of α.
2. The relative angular velocity $\Delta\omega$ of the cams is set to 0.5α.
3. The relative angular velocity $\Delta\omega$ of the cams is set to $1/\sqrt{2}\ \alpha$.
4. The relative phase $\Delta\theta$ between the cams is set to 0.5π rad.
5. The relative phase $\Delta\theta$ between the cams is set to $1/\sqrt{2}\pi$ rad.

Increasing or decreasing the rotation rates of both cams together has no effect on the mixing because of the previously demonstrated invariance of the flow to the Re (for $Re < 10$). Three different values for each of the two parameters ($\Delta\omega$ and $\Delta\theta$) were used, so that any trends in the resultant mixing would be evident. One of these values was chosen to be nonrational, since mixing rates are often increased by breaking symmetries in the flow.[27]

Figure 8 shows $\hat{M}_1$ and $\hat{M}_2$ vs. the work done $W(t)$ for the five different mixing conditions. Although some improvements can be obtained from varying the operating conditions, particularly for the cross-manifold mixing, these improvements are modest and in all cases the mixing rate across the manifolds is significantly lower than between the barrels of the mixer. For a well designed mixer, the mixing rate should be homogenous over the whole domain, leading to a similar evolution of both $\hat{M}_1$ and $\hat{M}_2$. However, even for $\Delta\omega = 0.5\alpha$, which results in the greatest performance increase, $\hat{M}_2$ is still 65–70% less than $\hat{M}_1$ for $W > 1.5 \times 10^{-4}$.

Figure 9 shows $M_2(\mathbf{x})$ at the end of the simulation ($W = 7.4 \times 10^{-4}$) for the new configurations. The spatial distribution of $M_2(\mathbf{x})$ for the four new configurations does not show any significant qualitative differences from the base case. In all cases, $M_2(\mathbf{x})$ is greatest within a figure-eight ridge that encircles the cams. The increase in $\Delta\hat{M}_2$ that is seen for the

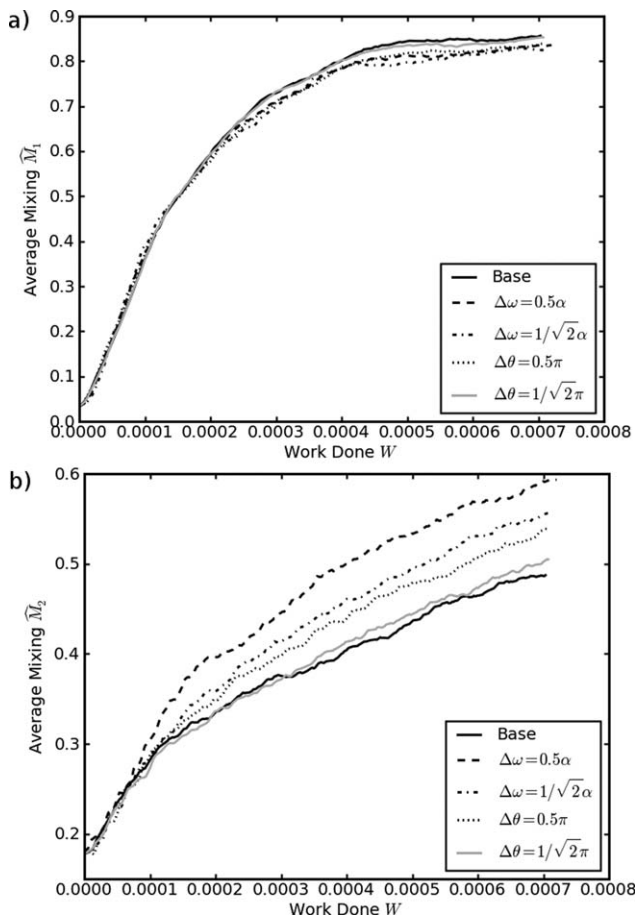

Figure 8. Average mixing measures (a) $\hat{M}_1$ and (b) $\hat{M}_2$ vs. work done by the mixer $W(t)$ (in J) for various mixer control values.

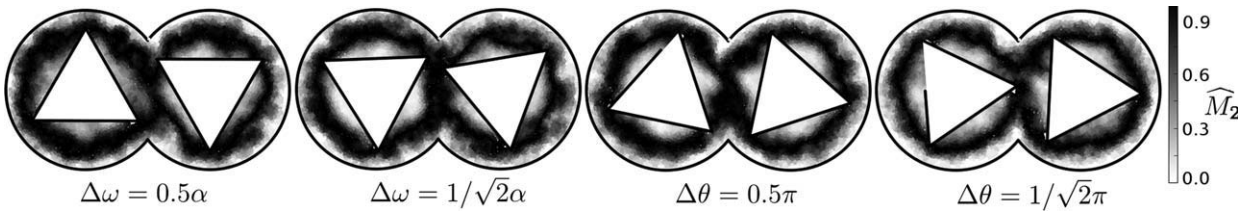

Figure 9. Spatial distribution of M_2(x) for each mixer configuration at $W = 7.4 \times 10^{-4}$ ($t = 934$ s for the base case).

new configurations corresponds to a proportional increase in the width of this ridge.

None of the operating condition changes have any observable effect on the structure of the manifold geometries. This is the reason why they do not significantly affect the speed or limit of the mixing process for this mixer. In all configurations, the flow around the cams is qualitatively similar, leading to the same basic figure eight manifold structure that was shown in Figure 4. This in turn leads to very similar areas of fluid being trapped between the manifolds and the cam walls which are unable to mix with the rest of the domain. Changes to operating conditions can modestly change the rate of the slowest component of mixing but cannot produce significant improvements. This requires changes to be made to the physical geometry of the mixer which then lead to more favorable structures of the manifolds.

Effect of changing cam geometry

Varying the geometry of the cams is a normal design response in mixer optimization. This section explores the relationship between the geometry of the cams and the chaotic manifolds of the flow that are responsible for determining the mixing performance. We consider three different geometric variations on the base Twin Cam mixer, all of which are shown in Figure 10. The first is a more angular version of the triangular cams, where one of the angles has been reduced to 30° (the other two angles are equal at 75°). The second uses thin, rectangular cams (blades), and the third mixer removes the central section from each rectangular cam.

The key dimensions of the mixers are marked in these figures. The remaining dimensions are the same for the original Twin Cam mixer. The simulated fluid is also identical, with a viscosity of 0.005 Pa s and a density of 1500 kg/m^3. All the Cams are rotated at 0.5 rpm, which gives $Re = 10$.

Geometry 1: Sharper isosceles triangular cams

This geometry is similar to the original Twin Cam mixer except that the equilateral triangular cams have been replaced with isosceles triangles. The apex angle of each isosceles triangle is 30° and the radius of each vertex from the barrel center is constant at 25.98 mm (this is the identical to the original equilateral cams)

Figure 11 shows the backwards time FTLE map using $T = -120$ s (one cam revolution) and $t_0 = 66$, 78, 96, and 114 s. Ridges in these FTLE plots show the location of the unstable (attractive) manifold. In a similar fashion, as for the original mixer geometry, the unstable manifold wraps around the cams in an approximate figure-eight structure. In contrast to the original simulation, a kink develops in the unstable manifold near the trailing long edge of the cams. A typical example of this is circled in the backwards time FTLE maps shown in Figure 11. This kink becomes more pronounced as the cam revolves through approximately one quarter of its period. The bottom left panel shows the FTLE map after 30 s ($t_0 = 96$ s), and it can be seen that the kink has grown larger and curls back in the opposite direction of the flow. The evolution of the flow involves fluid being attracted to and folded along the length of the unstable manifold. This manifold is also a Lagrangian structure and its movement is equivalent to the transport of a particular material line.

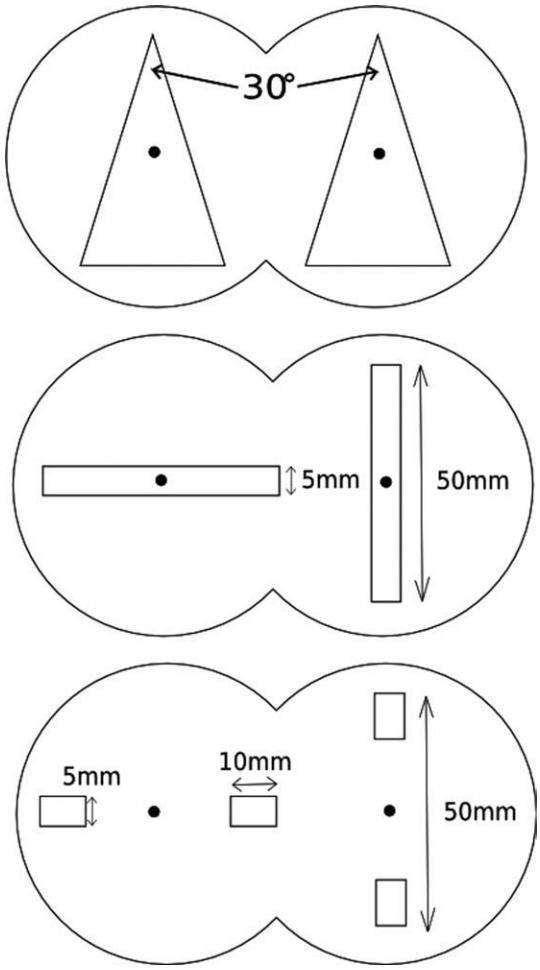

Figure 10. New Twin Cam geometries.

The basic structure of the Twin Cam mixer is preserved, only the shape of the Cams is altered.

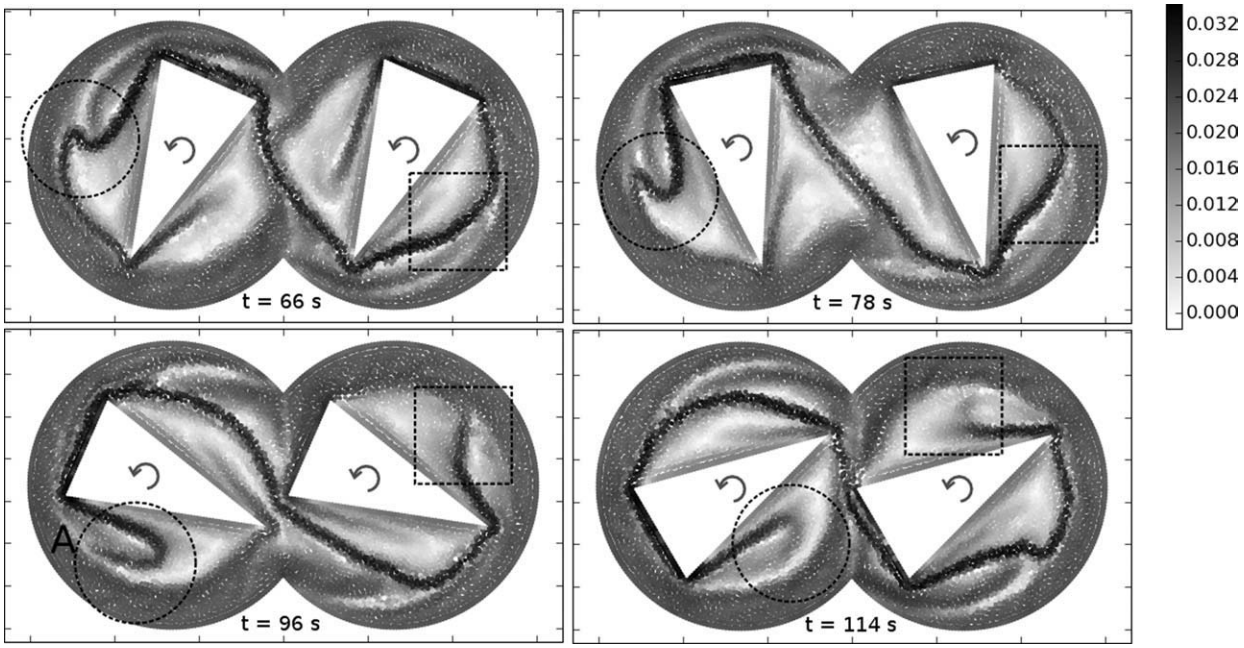

Figure 11. Backwards time FTLE map using $T = -120$ s for Geometry 1, shown at times $t = 66$, 78, 96, and 114 s.

Dark ridges in the FTLE plots show the location of the unstable (attractive) manifolds.

Therefore, the formation and subsequent growth of the kink in the unstable manifold indicates that the fluid originally between the manifold and the cam wall is being transported outward along the same path as the kink. At the same time, fluid that was originally on the other side of the manifold (i.e., between the manifold and the outer mixer boundary) is transported inwards. The developing kink has a similar shape as a breaking wave, with the fluid in the outer region moving in to fill the curl at the leading edge of the wave. The transport of fluid both inward and outward is significant and leads to strong mixing between the inner and outer regions that was lacking for the original equilateral triangle geometry.

Returning to the bottom left plot in Figure 11 ($t = 96$ s), it appears that the sharp corner at the leading edge of the wave structure (near label "A") has disappeared and that the continuous line of the manifold has been broken. However, this is a consequence of the FTLE estimates not capturing all the manifold structure, rather than any change in this structure. The accuracy of the FTLE estimation is limited near sharp corners, such as the leading edge of the kink. This is primarily a resolution issue, as very small changes in particle positions near these points can lead to very different dynamics over the time period T. Recall that the FTLE is calculated from the maximum stretching of a group of SPH particles with diameter $2h$ (the smoothing length h can be regarded as the resolution of the simulations and is equal to 1.3 times the average particle separation). A group of particles with diameter $2h$ that spans such a sharp manifold corner will be stretched out in multiple directions over the time period $t_0 < t < t_0 + T$. In contrast, a similar group of particles spanning a straight edge segment of the unstable manifold will only be stretched out along one main direction (i.e., tangential to the manifold). Therefore, the FTLE estimation for the former case will be less than the true value, while the latter case will be more accurate. Near label "A" in $t = 96$ s, this means that the ridge in the FTLE map disappears near the sharp corner of the manifold while the surrounding straight edges remain.

So far, the description of the manifold has centered on the evolution of the circled kink in Figure 11. A similar kink (highlighted using a dashed box) can also be seen near the leading edge of the right cam. However, this kink seems not as pronounced as the circled one and the manifold ridge is less well defined. This persists as the cams continue rotating. The kinks formed near the trailing edges of the cams are stronger than those near the leading edges. This indicates that the mixing near the leading edge is slightly weaker, leading to weaker stretching and folding movements of the fluid and therefore lower values of the FTLE. The difference between the flow near the leading and trailing edges is due to the triangular shape of the cams. When the fluid near the leading edge approaches the center of the mixer it interacts with the opposite cam. The orientation of this cam will be different for the fluid near the leading and trailing edges. In particular, when the fluid near the trailing edge approaches the center of the mixer, it passes much closer to one of the corners of the opposite cam. This enhances the mixing near the trailing edge of the first cam.

Figure 12 shows the mixing process between the inner and outer regions more explicitly, using colored particles to show the fluid transport. A circle of fluid with a radius from the center of each barrel equal to 22 mm is shaded dark gray and its evolution is tracked at times $t = 48$, 102, 132, and 156 s. These times were chosen to highlight the effect of the unstable manifold structure on the fluid particles near the trailing edge of the left cam. These particles are stretched out into a "breaking wave" shape that can be seen clearly in the bottom left corner at $t = 102$ s (label "A").

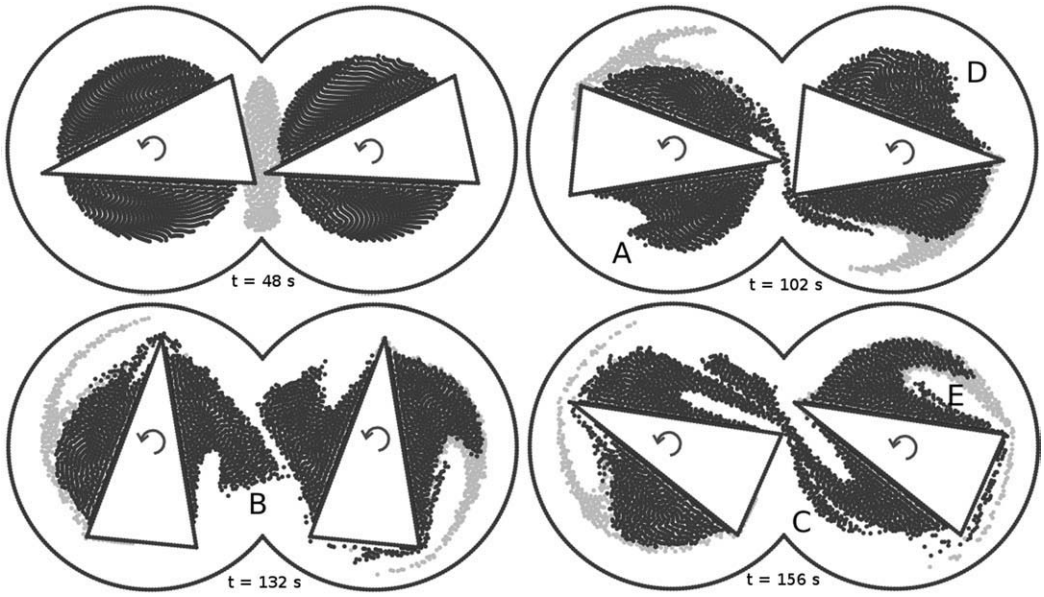

Figure 12. Sequence showing the transport of two different regions for Geometry 1.

The dark gray particles initially cover an area surrounded by a circle of radius 22 mm from the center of each cam. The light gray particles cover an area identical to the dyed region that was shown in Figure 3.

The plot at $t = 132$ s shows that these fluid particles (label "B"), are then stretched out until that are at a sufficient radius to approach the strong hyperbolic point at the center of the domain. This rapidly elongates the area of fluid, ripping away a significant portion and transporting it into the right barrel of the mixer (label "C"). Similar "breaking wave" structures can also be observed forming near the leading edges (e.g., Label "D"). However, these structures tend to form at a more slowly than those near the trailing edges and do not become as pronounced.

The light gray particles in Figure 12 also show the dyed region that was used to compare with the experimental results of Avalosse and Crochet.[4] The evolution of this region is largely similar to what was found with the equilateral triangles. The only significant change occurs near label "E," where a portion of the light gray particles is pulled inward and closer to the cam walls along the curl of the breaking wave shape formed by the dark gray particles.

The movement of the fluid between the inner and outer regions is the principle difference to the mixing process for this change in cam geometry. There is a large benefit in eliminating the dead zone close to the cam walls and therefore providing a more global, even distribution of mixing. The strength of this process (i.e., the speed at which the inner fluid particles are transported away from the cam walls) is dependent on the angle at the apex of the triangle. The sharper the triangle, the faster the inner region mixes with the rest of the domain. To show that this is the case, Figure 13 shows the change in unstable manifold structure using various values of apex angle ranging from 30° (i.e., Geometry 1) to 60° (i.e., original equilateral triangles). A slightly larger value of $T = 155$ s is used to ensure that the highlighted kink near the bottom left corner of the mixer is well defined, although it can be seen that this degrades the FTLE map for other sections of the domain, most notably near the center of the mixer. As the apex angle for the cams is increased, the size of the highlighted kink shrinks, indicating that a smaller area of fluid is being transported outward from between the manifold and the cam walls. In can also be seen that the kink in the manifold structure is present even in the original equilateral triangles, albeit much smaller.

Given that the strength of the inner/outer mixing process increases as the apex angle is reduced, it is reasonable to consider another cam geometry, where the triangular cams are replaced by very thin rectangular cams (or blades). The results in Figure 13 suggest that this change should maximize the extent and speed of the mixing process, producing more efficient mixing.

Geometry 2: Flat blade cams

Figure 14 shows the evolution of the backwards time FTLE map for a flat blade geometry ($T = -120$ s and $t_0 =$ 66, 79, 96, and 114 s). These are the same parameters used for Geometry 1 in Figure 11. Ridges in these maps again show the location of the unstable (attractive) manifolds. The shape and evolution of the resulting stable and unstable manifolds are qualitatively similar to that of Geometry 1. The thin rectangular cam is simply the asymptotic limit of a thin isosceles triangle and the geometry of the manifolds is therefore also similar. The stable and unstable manifolds circle the cams in an approximate figure-eight pattern, the size of which is comparable to the same figure-eight structure in Geometry 1 (i.e., this structure does not contract as the cam becomes narrower). Another similarity to Geometry 1 is the way the unstable manifold kinks near the long edges of each cam (see the circled manifold segment in each plot). However, for this geometry the kink is more exaggerated,

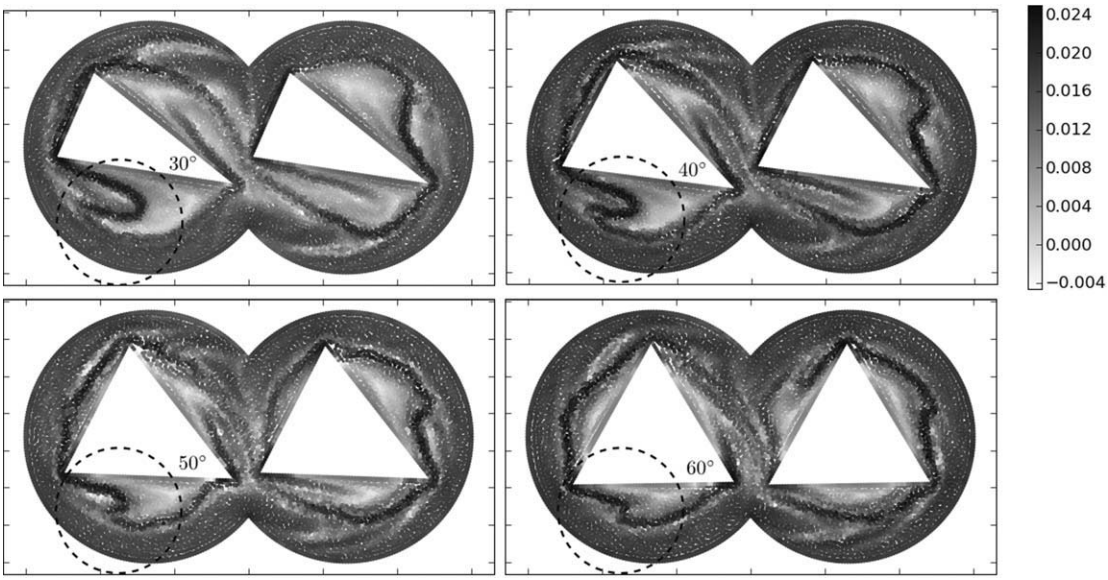

Figure 13. The backwards time FTLE maps for different values of the triangular cam apex angle, ranging from 30 to 60°.

The FTLEs were calculated using $t_0 = 96$ s and $T = 155$ s.

involves a larger area of fluid and occurs slightly earlier (the phase difference between the two events is about 25°).

For Geometry 1, it was observed that the mixing near the leading edge of the cam was different from that near the trailing edge, due to the differences in the proximity of the opposite cam that each fluid region comes in contact with as the cams rotate. Unlike Geometry 1, the cams for Geometry 2 are both horizontally and vertically symmetric. This means that the fluid on both sides of the cam interacts with the opposite cam in exactly the same way. Therefore, the mixing on both sides of the cam is identical, leading to a manifold structure that is also identical.

The increased area of fluid enclosed between the manifold structure and the cam boundary, as well as the increased size of the kink that develops as the cams rotate, both act to increase the area of fluid exchanged between the inner and outer regions of the mixer. Figure 15 shows the evolution of the same sets of particles that were shown in Figure 12. The wave structure that forms on either side of the cam is more exaggerated than for Geometry 1 and involves a larger exchange of fluid between the inner and outer regions. This can be seen most clearly by the evolution of a "finger" of white space (this structure is circled in each plot) into the inner region on both sides of each cam. This area of fluid is larger

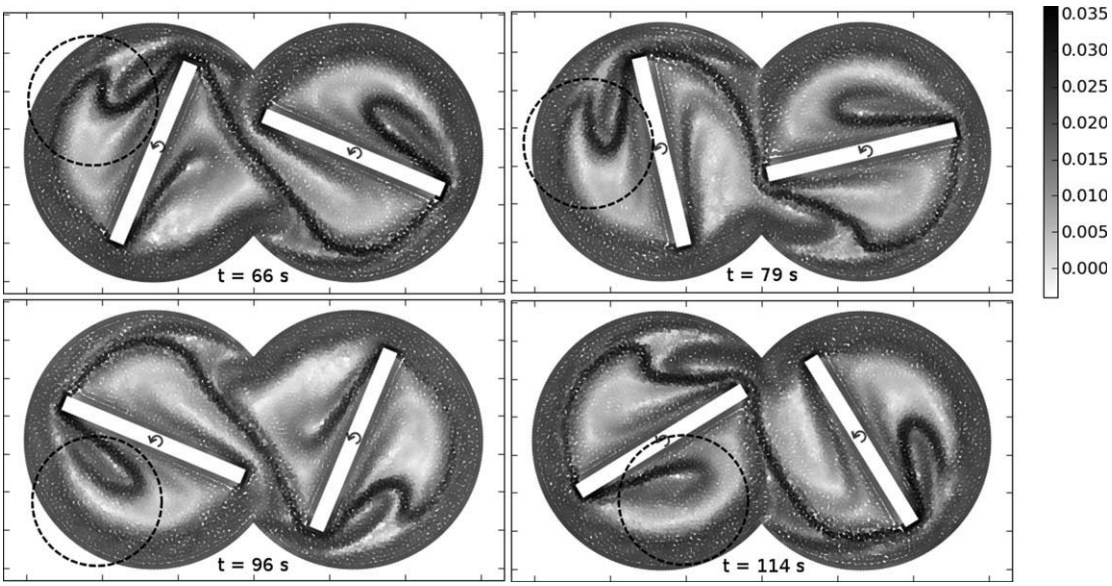

Figure 14. Backwards time FTLE map using $T = -120$ s for Geometry 2, shown at times $t = 66$, 79, 96, and 114 s.

Ridges in these plots show the unstable (attractive) manifold.

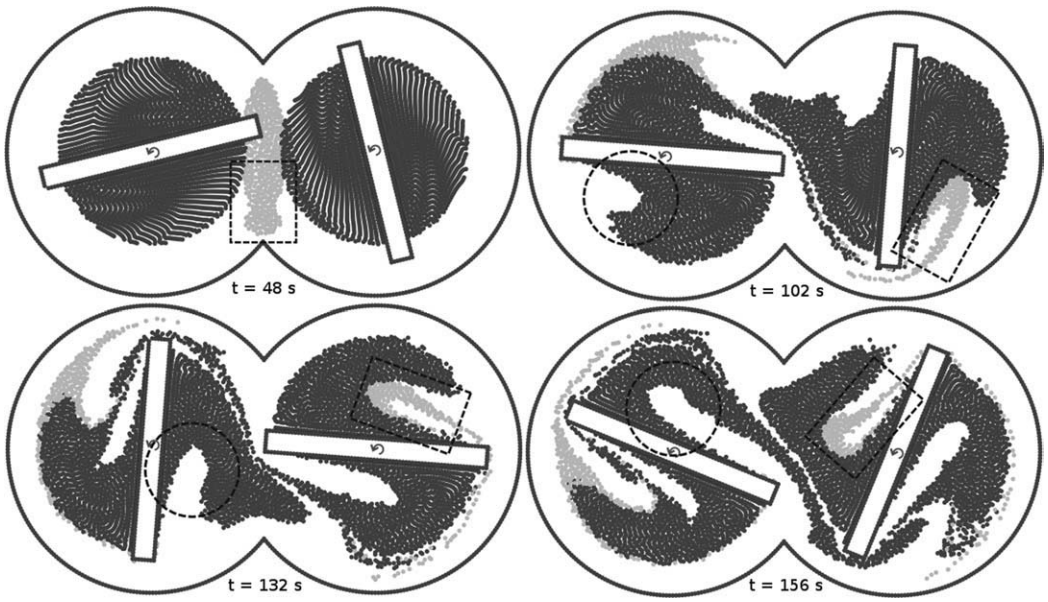

Figure 15. This sequence of plots shows how the flat blade cams transport the same initial set of particles that were used in Figure 12.

than the corresponding structure in Figure 12 and moves further along the edge of each cam during the same time period.

The light gray area initially in the center of the mixing helps us to see where some of this fluid originates. Following the movement of the lower portion of the light gray area in Figure 15 (highlighted using a dashed box) from a location close to the outer walls of the mixer, we see that it is transported into the bottom section of the right cam and into the curl of the wave structure that is forming with the dark gray fluid particles. It then moves inwards and across the length of the cam, eventually ending up near its center. After this time period ($\Delta t = 102$ s) it has moved radially inward a distance around half the radius of the cam barrel.

Geometry 3: Rotating blade tips

The final geometry that was considered is a variant of the thin rectangular blade cams, but with the central region of both cams removed. This allows fluid to flow in and around the center of both barrels, enabling the formation of two new stationary hyperbolic points in the flow, one located at each barrel center. As with the hyperbolic point at the center of the domain, each of these new points has its own stable and unstable manifold structure. In the following text, the stable and unstable manifolds belonging to the hyperbolic point at the center of the mixer will be referred to as S_C and U_C. The manifolds of the hyperbolic point in the left barrel are S_L and U_L, and those belonging to the hyperbolic point in the right barrel are S_R and U_R.

Figure 16 shows the evolution of the unstable (attractive) manifold for Geometry 3. The dominant manifolds are still S_C and U_C, as was the case for all the previous cam geometries. However, now the figure-eight structure is quite deformed due to the increased size of the kink that was first identified for Geometry 1. The kink starts to form in U_C early in the cam revolution and quickly grows in size (a typical example of this kink is circled in each plot). As a consequence of this growth, the manifold curves around each cam tip to penetrate into the center of each barrel (see label "A" in the FTLE plot at $t = 78$ s). This is in contrast to the previous geometry, where the cam boundary did not allow the fluid (and therefore the manifolds) to be transported into this region. The plots at $t = 96$ and 114 s show how the circled section of U_C continues to grow around the cam tip and along U_L. This manifold acts as a barrier, preventing U_C from moving further across the center of the barrel.

To properly describe the new manifolds (U_L, S_L, U_R, and S_R), it is necessary to see the structure of both the unstable and stable manifolds. Figure 17 (top) shows the forward and backwards time FTLE maps using $T = \pm 120$ s and $t_0 = 114$ s. Tracing the ridges of these maps gives the location of the stable and unstable manifolds. The bottom plot shows both of these manifolds overlayed on top of each other, allowing us to see the structure of both manifolds relative to each other. Each pair of manifolds intersect at their hyperbolic point (labels "A" in Figure 17) in a figure X configuration, the arms of which remain straight until they reach a radius comparable with the radius of the circle swept out by the cams. The stable manifolds then curve around in the direction of the flow, whereas the unstable manifolds curve in the opposite direction.

When the curved arms of the inner manifolds are near the outer left and right edges of the mixer, the unstable and stable manifolds are coincident. This can be seen in the top left and top right corners of the mixer shown in Figure 17, partially encircling the area colored light gray. When an unstable and stable manifold are coincident with each other, this indicates the presence of a strong barrier to advective fluid transport normal to this line. However, as the cams rotate, the manifolds rotate relative to each other. By the time the manifolds reach the center of the mixer, the angle between the two arms has grown until they cross each other almost at right angles (see label "B"). This large angle of intersection means that the manifolds no longer act as a mixing barrier and in fact

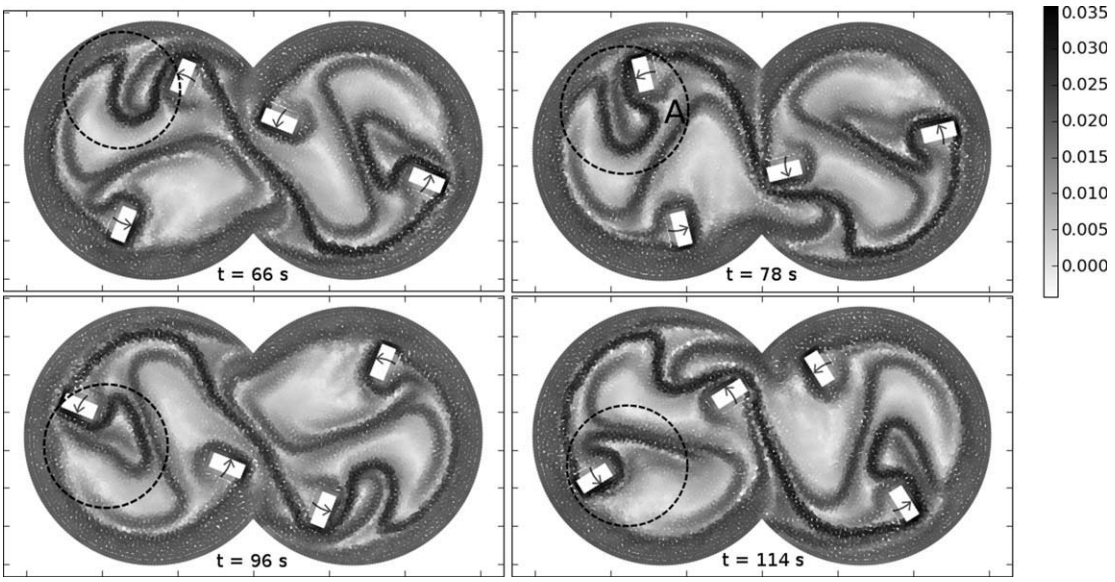

Figure 16. Backwards time FTLE map using $T = -120$ s for Geometry 3, shown at times $t = 66$, 78, 96, and 114 s.

Ridges in these plots show the unstable (attractive) manifold.

indicates strong local mixing. This is due to the right angle orientations of the local stretching and folding actions.

Figure 18 shows the evolution of the same colored particles as was previously shown for Geometries 1 and 2. These plots show how the changed mixing processes due to the removal of the central section of the cams enhance mixing in some regions and inhibit it in others. The new hyperbolic points at the center of each barrel promote strong local mixing. This can be seen from the elongated fluid structures near these points. However, as previously noted, the new manifolds are coincident while they are moving near the outer left and right walls of the mixer. This traps an enclosed lobe of fluid (colored light gray in Figure 17) that is 90° out of phase with the cams. To see how this affects the fluid transport, follow the evolution of the particles within the dashed circle in Figure 18. From $t = 48$ s to $t = 132$ s this area is trapped and does not mix effectively with the rest of the domain. Once the lobes rotate around to the centre of the mixer ($t = 156$ s), the manifolds in this region are no longer coincident and the particles are stretched out and start to mix with the rest of the domain. So, the entrapment of the fluid by the new manifolds is not constant over time and does not lead to the formation of any dead region, but it does delay the mixing of the fluid in this region.

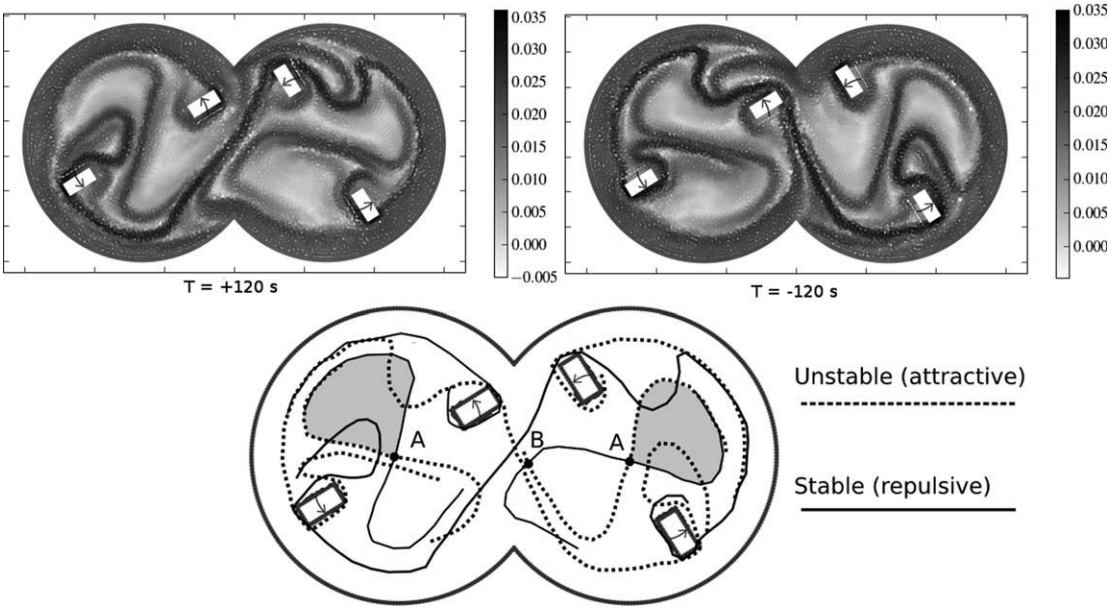

Figure 17. Top: Forward and backwards time FTLE spatial maps using $T = \pm 120$ s for Geometry 3; bottom: The unstable (dotted lines) and stable (solid lines) manifolds which have been generated by tracing out the ridges in the above FTLE plots.

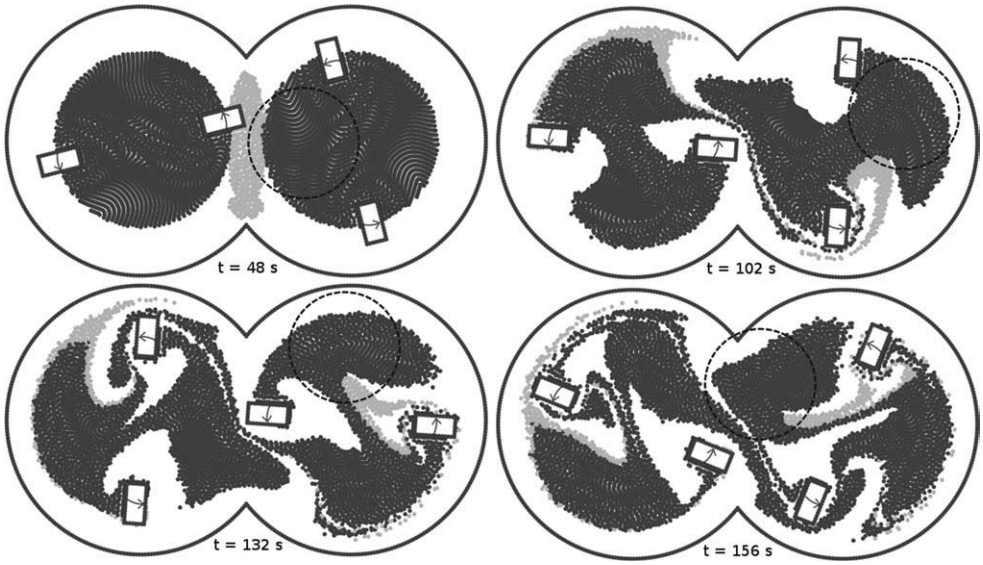

Figure 18. This shows how Geometry 3 transports the same initial set of particles that were shown in Figure 12.

Whether or not this new cam geometry is beneficial overall to the efficiency of the mixing is unclear from these results. The mixing is enhanced in some areas (near the center of each barrel), but inhibited in others (the lobes located 90° out of phase with the cams). To quantitatively compare the mixing produced by the different cam geometries we will next consider the evolution of the mixing measures $\hat{M}_1$ and $\hat{M}_2$.

Quantitative mixing comparison

Figure 19 shows plots of $\hat{M}_1$ (top) and $\hat{M}_2$ (bottom) vs. time for the four (three new plus the original) cam geometries. As explained earlier, $\hat{M}_1$ is a measure of the average amount of mixing between the two barrels of the Twin Cam mixer and $\hat{M}_2$ measures the average amount of mixing between the inner region (defined as the area within a radius of 22 mm of the center of each barrel) and the rest of the domain. Figure 20 shows the spatial distribution of $M_1(\mathbf{x})$ and $M_2(\mathbf{x})$ for Geometry 2 at times $t = 0$, 107, 300, and 589 s.

The evolution of the mixing measure $\hat{M}_1$ has three main stages. From $0 < t < 200$ s the increase of $\hat{M}_1$ is greatest and all four geometries show a roughly linear increase. This period covers the first 1.75 rotations of the cams. Over this time, the particle colors are still separated into distinct regions and the increase of $\hat{M}_1$ directly relates to the elongation of the interface between these regions. A typical example of the spatial distribution of $M_1(\mathbf{x})$ during this time period can be seen at $t = 107$ s in Figure 20. All the geometries show a similar mixing performance over this time period. The base geometry results in a slightly higher value of $\hat{M}_1$, however, this is due to the larger cam displacing a greater area of unmixed fluid.

After $t \approx 200$ s, the rate of increase of $\hat{M}_1$ begins to slow and become a little noisier. The interface between the color regions is now much less defined and there are many small

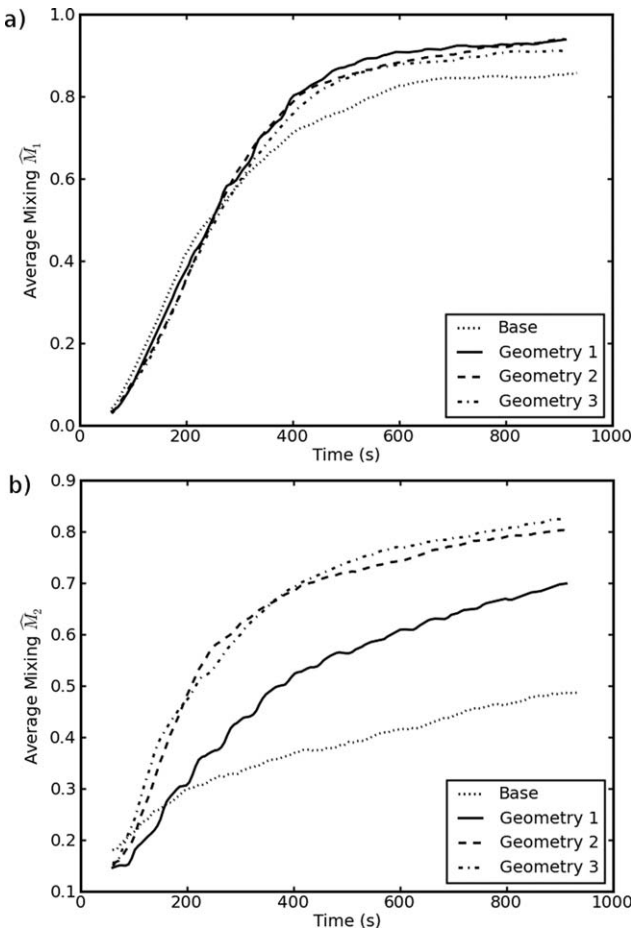

Figure 19. Average mixing measures (a) $\hat{M}_1$ and (b) $\hat{M}_2$ vs. time for the four different cam geometries.

$\hat{M}_1$ is a measure of the average mixing between the two barrels of the Twin Cam mixer. $\hat{M}_2$ is a measure of the average mixing between the inner and outer regions.

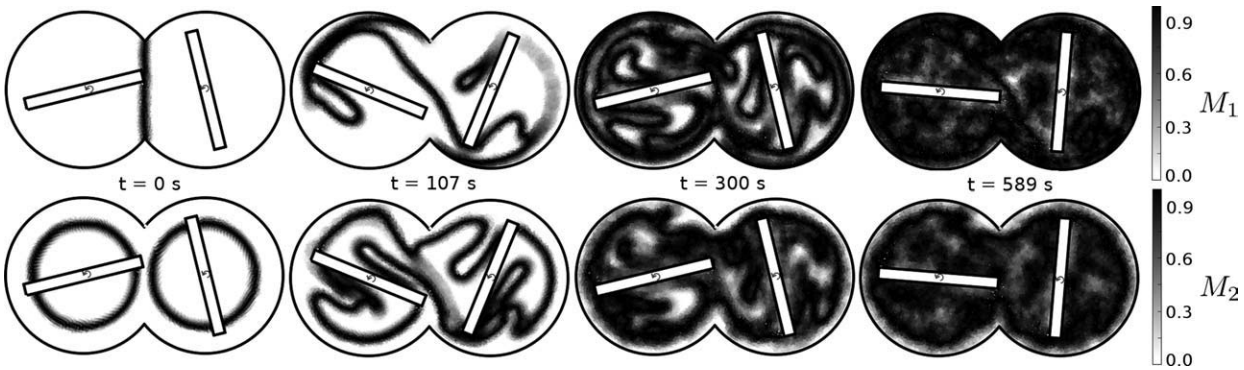

Figure 20. M_1(x) (top row) and M_2(x) (bottom row) for Geometry 2.

clumps of light and dark particles distributed through the domain. The mixing measure $\hat{M}_1$ now relates more to the relative concentrations of colors throughout the domain rather than the length of the interface between the color regions.

From $t > 400$ s, the differences in mixing performance of the alternative geometries becomes clear. $\hat{M}_1$ for the base case geometry levels off more quickly than for the other geometries and eventually asymptotes to a value of $\hat{M}_1 = 0.85$, which is significantly lower than for the alternative geometries. During this last phase of the mixing, the interface between the color regions have all but disappeared and the different colors are now randomly distributed throughout the domain, more highly concentrated in some regions and less in others. The differences in $\hat{M}_1$ between all three of the new alternative geometries considered are not significant. They are all essentially equally able to mix fluid between the different barrels. The clear performance gap that develops between the original and new geometries for longer times is related to the mixing of the inner fluid region which is isolated by the closed figure-eight manifold structure of the flow. All of the new geometries (to varying degrees) allow this region to mix more efficiently with the rest of the domain.

The plots of $\hat{M}_2$ clearly show the improvement in mixing between the inner and outer regions when changing the cam geometry. The original equilateral triangular cams give by far the poorest result with the slowest mixing. By the end of the simulation the value of $\hat{M}_2$ has not yet reached 0.5. Conversely, Geometry 1 shows a significant improvement, with the extent of mixing rising much faster and reaching 0.7 by the same time. This is due to the additional mixing that the isosceles cams introduce between the inner and outer regions by creating the larger kink structure in the manifold. The mixing process improves as the cam apex angle is reduced. In the limit of a flat blade (Geometry 2) we observe significantly faster mixing with the measure $\hat{M}_2$ reaching 0.8 at the end of the simulation.

Although the mixing between the inner and outer regions in Geometry 2 is significantly improved over that of the original equilateral triangles, there is still an area close to the outer boundary that is not mixed as effectively as the rest of the domain. Compare the plots of $M_1(\mathbf{x})$ and $M_2(\mathbf{x})$ in Figure 20 at $t = 589$ s. By this time $M_1(\mathbf{x})$ is roughly homogenous throughout the entire domain, but $M_2(\mathbf{x})$ still has a thin area of white next to the outer boundary. Ideally, a well designed mixer would have a equal mixing rate over the entire domain, with no one regions particularly isolated from another. This would be reflected in the plots of $\hat{M}_1$ and $\hat{M}_2$ as an identical increase of these average values over time.

The mixing performance of Geometry 3 is very similar to that of Geometry 2. According to $\hat{M}_2$, it is slightly better early in the process, slightly less fast in the middle stages and then modestly faster in the later stages. It therefore appears that the additional hyperbolic points that are introduced with this geometry have a very weakly net positive effect on the mixing. These points tend to enhance the mixing near the center of each barrel (leading to faster mixing early in the process) while inhibiting it in the lobes identified in the previous section leading to the slightly slower mixing in the middle stages of the process. These two effects seem to largely cancel each other out. Whilst $\hat{M}_2$ for Geometry 3 is slightly higher than Geometry 2 for much of the simulation, this does not mean that Geometry 3 will be universally better. Choosing different spatial distributions for the colors may marginally favor different cam shapes depending on whether the concentration of like material are in areas of strong mixing or not. On this basis we cannot reasonably differentiate a meaningful performance difference between the two blade variations.

Conclusion

This article has explored the effect of altering the cam geometry and relative motion on the mixing efficiency and chaotic manifold structure for a Twin Cam mixer. Previously, the mixing has been shown to be invariant to the Reynolds number and therefore synchronized speed changes of the cam rotation do not change the nature or extent of the mixing produced. Here, we also explored the effect of operating condition changes, such as differential cam speeds and phase offsets. These changes resulted in a modest improvement in the mixing across the manifold boundary, noticeably stronger for the cases involving differential cam speeds. However, in all cases, operating variations using the original equilateral cams were found to have little effect on manifold geometry or the qualitative description of the mixing processes.

Changing the geometry of the cams produced a range of new mixing behaviors. In the original mixer with equilateral cams, a dead zone was identified between the stable and unstable manifolds and the cam walls. However, reducing the angle of the triangle apex resulted in a significant increase of fluid transfer in and out of this dead zone. This was indicated via the growth of a kink in the manifold

structure. This kink grew outward from the dead zone, drawing with it fluid from this inner region. Within the duration of one cam revolution, a significant amount of this fluid was at a sufficient radius from the center of each cam to interact with the strong hyperbolic point at the center of the mixer. This rapidly elongated the area of fluid contained by the kink and divided it between the two barrels of the mixer. Reducing the size of the apex angle increased the area encompassed by the kink and therefore increased the amount of fluid transfer in and out of the inner region. This leads to steadily improving mixing performance. The most efficient mixing was produced by the thin rectangular cams which maximized the mixing between the inner and outer regions in each barrel of the mixer.

The last cam geometry examined was a pair of blade tips rotating around the center of each barrel of the mixer. This allowed fluid to flow across the center of each barrel, resulting in the formation of two additional stationary hyperbolic points located at the centre of each barrel. Each of these hyperbolic points formed its own stable and unstable manifolds. Although each hyperbolic point resulted in a strong mixing locally, the manifold structure showed that a large lobe of fluid located 90° out of phase with the cams was trapped during half of each cam rotation, slowing the mixing of this region. The quantitative mixing measures M showed that this cam geometry had similar mixing efficiency to the full flat blade cams.

The time-varying structure of the manifolds is fundamental to understanding the short-time transient nature of any chaotic flow, and as such they provide a useful analysis technique for the design of an industrial mixer. The numerical tools used in this article (SPH and FTLE) are flexible and can be applied to time-varying, nonperiodic flows and mixers with complicated moving geometry and free-surfaces. Extending these techniques to 3D will provide additional challenges, mostly involving the extraction and visualization of the 2D manifold surfaces. However, existing results[24] show that visualizing the manifold surfaces in a 3D flow can be reliably achieved.

Notation

t = time
t_0 = start time for the finite-time Lyapunov exponent calculation
T = integration time for FTLE calculation
σ = FTLE
$\mathbf{x}$ = position
$M(\mathbf{x})$ = mixing measure
L = length scale used to calculate $M(\mathbf{x})$
$\hat{M}$ = average $M(\mathbf{x})$ over the entire domain
$W(t)$ = work done by the twin cam mixer

Literature Cited

1. Ottino J. *The Kinematics of Mixing: Stretching, Chaos and Transport*. Cambridge: Cambridge University Press, 1989.
2. Robinson M, Cleary P, Monaghan J. Analysis of mixing in a Twin-Cam mixer. *AIChe J*. 2008;8:1987–1998.
3. Avalosse T, Crochet M. Finite-element simulations of mixing: 1. Two-dimensional flow in periodic geometry. *AlChE J*. 1997;3:577–587.
4. Bertrand F, Thibault F, Delamare L, Tanguy P. Adaptive finite element simulation of fluid flow in twin-screw extruders. *Comput Chem Eng*. 2003; 491–500.
5. Jana SC, Metcalfe G, Ottino JM. Experimental and computational studies of mixing in complex stokes flows: the Vortex mixing flow and multicellular cavity flows. *J Fluid Mech*. 1994;269:199–246.
6. Monaghan J. Smoothed particle hydrodynamics. *Rep Prog Phys*. 2005;68:1703–1759.
7. Metcalfe G, Rudman M, Brydon A, Graham LJW, Hamilton R. Composing chaos: an experimental and numerical study of an open duct mixing flow. *AIChE J*. 2006;1:9–28.
8. Wiggins S. *Chaotic Transport in Dynamical Systems*. New York: Springer-Verlag, 1992.
9. Shadden SC, Lekien F, Marsden JE. Definition and properties of Lagrangian coherent structures from finite-time Lyapunov exponents in two-dimensional aperiodic flows. *Physica D Nonlinear Phenomena*. 2005;212:271–304.
10. Hobson D. An efficient method for computing invariant manifolds of planar maps. *J Comput Phys*. 1993;1:14–22.
11. Pierrehumbert RT, Yang H. Global chaotic mixing on isentropic surfaces. *J Atmosph Sci*. 1993;15:2462–2480.
12. Aldridge BB, Haller G, Sorger PK, Lauffenburger DA. Direct lyapunov exponent analysis enables parametric study of transient signaling governing cell behavior. *IEE Proc Syst Biol*. 2006;6:425–432.
13. Monaghan J, Kos A, Issa N. Fluid motion generated by impact. *J Waterway Port Coast Ocean Eng*. 2003;6:250–259.
14. Cole R. *Underwater Explosions*. Princeton, NJ: Princeton University Press, 1948.
15. Monaghan JJ. SPH and Riemann solvers. *J Comput Phys*. 1997; 136:298–307.
16. Shamekhi A, Sadeghy K, Bahrami MN, Naei MH. Using mesh free method for numerical simulation of non-newtonian fluid flow over a step. *J Soc Rheol Jpn*. 2008;36:19–27.
17. Shao S, Lo E. Incompressible sph method for simulating newtonian and non-newtonian flows with a free surface. *Adv Water Resources*. 2003;26:787–800.
18. Laigle D, Lachamp P, Naaim M. Sph-based numerical investigation of mudflow and other complex fluid flow interactions with structures. *Comput Geosci*. 2007;11:297–306.
19. Rodriguez-Paz MX, Bonet J. A corrected smooth particle hydrodynamics method for the simulation of debris flows. *NMPDE*. 2004;20:140–163.
20. Hosseini SM, Manzari MT, Hannani SK. A fully explicit three-step SPH algorithm for simulation of non-newtonian fluid flow. *Int J Numer Methods*. 2007;17:715–735.
21. Ellero M, Tanner R. SPH simulations of transient viscoelastic flows at low reynolds number. *J Non-Newtonian Fluid Mech*. 2005; 132:61–72.
22. Cleary PW, Prakash M, Ha J, Stokes N, Scott C. Smooth particle hydrodynamics: status and future potential. *Progr Comput Fluid Dyn*. 2007; 70–90.
23. Lapeyre G. Characterization of finite-time Lyapunov exponents and vectors in two-dimensional turbulence. *Chaos*. 2002;3:688–698.
24. Sadlo F, Peikert R. Visualizing Lagrangian coherent structures and comparison to vector field topology. *Topology-Based Methods in Visualization II*. 2009;2:15–29.
25. Poux M, Fayolle P, Bertand J, Bridoux D, Bousquet J. Powder mixing: some practical rules applied to agitated systems. *Powder Technol*. 1991;68:213–234.
26. Ryrie SC. Mixing by chaotic advection in a class of spatially periodic flows. *J Fluid Mech*. 1992;236:1–26.
27. Voth GA, Saint TC, Dobler G, Gollub JP. Mixing rates and symmetry breaking in two-dimensional chaotic flow. *Phys Fluids*. 2003; 15:2560–2566.

Manuscript received Aug. 13, 2009, revision received Jan. 28, 2010, and final revision received May 18, 2010.